Journal of Fluids and Structures 17 (2003) 365–380

JOURNAL OF FLUIDS AND STRUCTURES

www.elsevier.nl/locate/jnlabr/yjfls

Flow-induced force fluctuations on a sphere at high Strouhal number

J. Wang[a,*], G.C. Lauchle[b], M.S. Howe[c]

[a] *The Trane Company, 3600 Pammel Creek Road, La Crosse, WI 54601, USA*
[b] *The Pennsylvania State University, Graduate Program in Acoustics and Applied Research Laboratory, P.O. Box 30, State College, PA 16804, USA*
[c] *Boston University, College of Engineering, 110 Cummington Street, Boston, MA 02215, USA*

Received 10 March 2001; accepted 3 October 2002

Abstract

An empirical model is developed to estimate the broadband unsteady force spectrum induced on a rigid sphere in a nominally steady, uniform flow. The Reynolds number is sub-critical, and the frequency range considered is above the low-mode Strouhal shedding frequency of the sphere ($0.5 \leqslant fd/U_0 \leqslant 100$, where f is the frequency, d is the diameter, and U_0 is the mean flow speed). The model uses the separation of variables assumption for the cross-power spectral densities of the surface pressure fluctuations. The assumption is shown to be a proper engineering approximation except in the lower part of the considered frequency range. In addition, the flow-induced unsteady lift and drag forces are measured independently of each other using towed spheres in a basin of water. Both estimations, from the empirical model and the data measured in the tow tank, show that the dimensionless power spectral densities of broadband unsteady lift and drag forces are constant for $fd/U_0 < 1$, and $(fd/U_0)^{-3}$ dependent for $1 \leqslant fd/U_0 \leqslant 100$. The model predicts that the broadband spectral density of the unsteady lift force is about 5 dB higher than that of the unsteady drag force, while the measured data show the level difference between 3 and 7 dB. The empirical model presented here has application in predicting the flow-induced noise of underwater hydrophones that sense acoustic particle velocity or acceleration.

1. Introduction

Underwater acoustic sensors that respond to acoustic pressure are known as pressure hydrophones. Sensors that respond to the acoustic particle velocity, or particle acceleration are called velocity, acceleration, or pressure gradient hydrophones. The typical velocity (or acceleration) sensor in use today is basically composed of a geophone (or accelerometer) encased in a neutrally buoyant body, which will move with the fluid particles as an acoustic wave passes by it. Thus, these sensors are also called inertial sensors, e.g., Gabrielson et al. (1995). The subject of this paper is the flow-induced noise on inertial sensors configured as spheres. A flow of interest might be generated by low-velocity (less than 1 knot) ocean currents or wave motion. In practice, the diameter of the sensor is chosen with knowledge of the typical flow velocity range, to assure that the Strouhal shedding frequency of the sensor is well below the operational frequency range of the sensor. Consequently, the frequency range of interest is well above the sensor shedding frequency and the spectrum is broadband. Here, high frequencies are defined as those that are above Strouhal shedding frequency of the sensor body.

*Corresponding author. Tel.: +1-608-787-4181; fax: +1-608-787-2669.
E-mail address: jjwang@trane.com (J. Wang).

0889-9746/03/$ - see front matter
PII: S0889-9746(02)00139-1

The high-frequency flow-induced noise on a sensor can be attributed to one or more of three different sources: (i) unsteadiness due to the vortex formation process in the near wake of the sensor, (ii) surface pressure fluctuations generated by transitional, separated, and turbulent boundary-layer flow, and (iii) free-stream turbulence. All of these sources produce pressure fluctuations on the surface of the sensor that, when integrated, yield an unsteady force. The level and frequency content of an inertial sensor output is proportional to the spectrum of this unsteady force because of Newton's second law.

McEachern and Lauchle (1995) showed that the flow-induced noise measured on neutrally buoyant acoustic velocity sensors configured as cylinders in cross-flow is indeed proportional to the hydrodynamic force fluctuations. Lauchle and Jones (1998) demonstrated the same conclusion for a spherical velocity sensor. In both sets of experiments—the former in a flooded quarry, and the latter in a tow tank—free-stream turbulence was nonexistent. The near-wake turbulence and the natural boundary layer development on the surface of the sensor established a fundamental lower limit of flow noise in these previous experiments.

We continue this previous research here under the assumptions that the sensor is spherical, the flow is sub-critical (laminar boundary layer separation on the sphere triggers turbulent wake formation), and the free-stream turbulence is negligible. The goal is to develop an empirical model for the unsteady force spectra (side, lift, and drag components). This model is to be verified with the force spectra calculated from the measured data in a tow tank experiment. In addition, we also compare with a recently developed ring vortex model for the force fluctuations on a sphere (Howe et al., 2001), where the force is calculated by modelling the wake as a series of randomly oriented vortex rings of equal circulation. The empirical analysis given in this paper is based on integrating the wall pressure fluctuations over the sphere surface. These pressure fluctuations are assumed to be due to the separation of the laminar boundary layer and the subsequent formation of vorticity in the near wake. The two-point statistics of these pressure fluctuations are measured in a wind tunnel experiment. The reader is referred to Lauchle and Jones (1998), Wang (1999), and Howe et al. (2001) for complete bibliographies of previously published work on the unsteady force acting on spheres in a steady, uniform flow.

2. Empirical analysis

In the following, Reynolds number is defined as $\mathrm{Re} = U_0 d/\nu$, where d is the sphere diameter, U_0 is the free-stream flow velocity, and ν is the kinematic viscosity. The empirical model is for the two-point statistics of wall pressure fluctuations and their integration over the sphere surface under sub-critical flow conditions ($3000 \leqslant \mathrm{Re} \leqslant 370{,}000$). It is proven in Wang (1999) that the wall shear stress fluctuations contribute negligibly to the forces predicted and measured in this Re range. All physical quantities are assumed to be stationary in time.

The coordinate system is illustrated in Fig. 1. Given a surface pressure fluctuation $p(\theta, \phi, t)$ on the sphere of radius a, the rectangular components of the unsteady force are:

$$f_x(t) = \iint [p(\theta,\phi,t)\,\mathrm{d}S]\cos\theta = a^2 \int_0^{2\pi}\int_0^{\pi} p(\theta,\phi,t)\sin\theta\cos\theta\,\mathrm{d}\theta\,\mathrm{d}\phi, \tag{1a}$$

$$f_y(t) = a^2 \int_0^{2\pi}\int_0^{\pi} p(\theta,\phi,t)\sin^2\theta\sin\phi\,\mathrm{d}\theta\,\mathrm{d}\phi, \tag{1b}$$

$$f_z(t) = a^2 \int_0^{2\pi}\int_0^{\pi} p(\theta,\phi,t)\sin^2\theta\cos\phi\,\mathrm{d}\theta\,\mathrm{d}\phi, \tag{1c}$$

where $-f_x(t)$, $f_y(t)$, and $f_z(t)$ are, respectively, the unsteady drag, side and lift force. These forces are then Fourier transformed and cast into coefficient forms:

$$\tilde{C}_x(\omega) = \frac{\tilde{F}_x(\omega)}{\pi a^2 q} = \frac{1}{\pi q}\int_0^{2\pi}\int_0^{\pi} \tilde{P}(\theta,\phi,\omega)\sin\theta\cos\theta\,\mathrm{d}\theta\,\mathrm{d}\phi, \tag{2a}$$

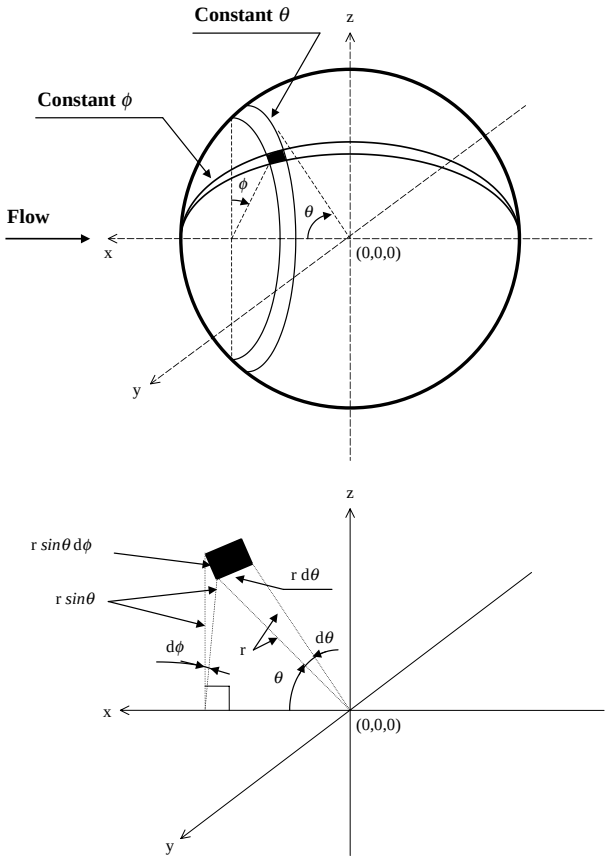

Fig. 1. Three-dimensional illustration of the spherical coordinate system.

$$\tilde{C}_y(\omega) = \frac{\tilde{F}_y(\omega)}{\pi a^2 q} = \frac{1}{\pi q}\int_0^{2\pi}\int_0^{\pi} \tilde{P}(\theta,\phi,\omega)\sin^2\theta\sin\phi\,\mathrm{d}\theta\,\mathrm{d}\phi, \tag{2b}$$

$$\tilde{C}_z(\omega) = \frac{\tilde{F}_z(\omega)}{\pi a^2 q} = \frac{1}{\pi q}\int_0^{2\pi}\int_0^{\pi} \tilde{P}(\theta,\phi,\omega)\sin^2\theta\cos\phi\,\mathrm{d}\theta\,\mathrm{d}\phi, \tag{2c}$$

where tilde denotes a complex quantity, $q = \rho U_0^2/2$, ρ is the fluid density, and $-\infty < \omega < \infty$. The two-sided auto-power spectral density function of the unsteady drag coefficient is

$$\Phi_x(\omega) = \tilde{C}_x^*(\omega)\tilde{C}_x(\omega) = |\tilde{C}_x(\omega)|^2 = \frac{1}{\pi^2 q^2}\int_0^{2\pi}\int_0^{2\pi}\int_0^{\pi}\int_0^{\pi} \tilde{\Phi}_{12}(\theta_1,\phi_1,\theta_2,\phi_2,\omega)\sin\theta_1\cos\theta_1\sin\theta_2\cos\theta_2\,\mathrm{d}\theta_1\,\mathrm{d}\theta_2\,\mathrm{d}\phi_1\,\mathrm{d}\phi_2, \tag{3}$$

where the star denotes the complex conjugate, and $\tilde{\Phi}_{12}(\theta_1,\phi_1,\theta_2,\phi_2,\omega) = \tilde{P}^*(\theta_1,\phi_1,\omega)\tilde{P}(\theta_2,\phi_2,\omega)$ is the two-sided cross-power spectral density of the surface pressure fluctuations. Following the notation of Bendat and Piersol (2000), the spectral quantities are changed from two-sided to one-sided, i.e., $G_x = 2\Phi_x$ and $\tilde{G}_{12} = 2\tilde{\Phi}_{12}$. This permits the model to be compared to experimental spectra measured at only positive frequencies. In converting frequency to Strouhal

number, $\mathscr{S}t = fd/U_0$, $G_x(f)$ must be further normalized by the time scale (d/U_0):

$$G_x(\mathscr{S}t) = G_x(f)\left(\frac{U_0}{d}\right) = \frac{1}{\pi^2}\int_0^{2\pi}\int_0^{2\pi}\int_0^{\pi}\int_0^{\pi}\{\tilde{G}_{12}(\theta_1,\phi_1,\theta_2,\phi_2,\mathscr{S}t)\}\sin\theta_1\cos\theta_1\sin\theta_2\cos\theta_2\,\mathrm{d}\theta_1\,\mathrm{d}\theta_2\,\mathrm{d}\phi_1\,\mathrm{d}\phi_2. \quad (4)$$

Note that U_0/q^2d is grouped with $\tilde{G}_{12}$ such that $\tilde{G}_{12}(\theta_1,\phi_1,\theta_2,\phi_2,\mathscr{S}t) = \tilde{G}_{12}(\theta_1,\phi_1,\theta_2,\phi_2,\mathscr{S}t)U_0/q^2d$.

By changing variables from (ϕ_1,ϕ_2) to (ϕ_1,ϕ_d), where $\phi_d = \phi_2 - \phi_1$, and using trigonometric properties, the force auto-spectra become:

$$G_x(\mathscr{S}t) = \frac{1}{4\pi^2}\int_0^{2\pi}\int_{-\phi_1}^{2\pi-\phi_1}\int_0^{\pi}\int_0^{\pi}\{\tilde{G}_{12}(\theta_1,\theta_2,\phi_1,\phi_d,\mathscr{S}t)\}\sin 2\theta_1\sin 2\theta_2\,\mathrm{d}\theta_2\,\mathrm{d}\theta_1\,\mathrm{d}\phi_d\,\mathrm{d}\phi_1, \quad (5a)$$

$$G_y(\mathscr{S}t) = \frac{1}{2\pi^2}\int_0^{2\pi}\int_{-\phi_1}^{2\pi-\phi_1}\int_0^{\pi}\int_0^{\pi}\{\tilde{G}_{12}(\theta_1,\theta_2,\phi_1,\phi_d,\mathscr{S}t)\}\sin^2\theta_1\sin^2\theta_2[\cos\phi_d - \cos(2\phi_1+\phi_d)]\,\mathrm{d}\theta_2\times\mathrm{d}\theta_1\,\mathrm{d}\phi_d\,\mathrm{d}\phi_1, \quad (5b)$$

$$G_z(\mathscr{S}t) = \frac{1}{2\pi^2}\int_0^{2\pi}\int_{-\phi_1}^{2\pi-\phi_1}\int_0^{\pi}\int_0^{\pi}\{\tilde{G}_{12}(\theta_1,\theta_2,\phi_1,\phi_d,\mathscr{S}t)\}\sin^2\theta_1\sin^2\theta_2[\cos\phi_d + \cos(2\phi_1+\phi_d)]\,\mathrm{d}\theta_2\,\mathrm{d}\theta_1\mathrm{d}\phi_d\,\mathrm{d}\phi_1. \quad (5c)$$

Because the incident flow is uniform and the bluff body is a sphere, rotation of the coordinate system in the ϕ-direction does not change the physical results. The cross-power spectral density $\tilde{G}_{12}$ is, therefore, homogeneous in the ϕ-direction:

$$\begin{aligned}\langle\tilde{G}_{12}(\theta_1,\theta_2,\phi_1,\phi_2,f)\rangle &= \langle P^*(\theta_1,\phi_1,f)P(\theta_2,\phi_2,f)\rangle\\ &= \langle P^*(\theta_1,\phi_1+\phi_r,f)\,P(\theta_2,\phi_2+\phi_r,f)\rangle,\end{aligned} \quad (6)$$

where the angle bracket $\langle\ \rangle$ denotes ensemble average over many measurements and ϕ_r is the angle of rotation. Homogeneity of $\tilde{G}_{12}$ in the ϕ-direction implies that $\tilde{G}_{12}$ depends on the separation angle, ϕ_d, but not on the reference angle, ϕ_1. Thus, $G_z(\mathscr{S}t)$, and $G_y(\mathscr{S}t)$, are equal. Eqs. 5(a)–(c) become

$$G_x(\mathscr{S}t) = \frac{1}{4\pi^2}\int_0^{2\pi}\int_{-\phi_1}^{2\pi-\phi_1}\int_0^{\pi}\int_0^{\pi}\{\langle\tilde{G}_{12}(\theta_1,\theta_2,\phi_d,\mathscr{S}t)\rangle\}\sin 2\theta_1\sin 2\theta_2\,\mathrm{d}\theta_2\,\mathrm{d}\theta_1\,\mathrm{d}\phi_d\,\mathrm{d}\phi_1, \quad (7a)$$

$$G_y(\mathscr{S}t) = G_z(\mathscr{S}t) = \frac{1}{2\pi^2}\int_0^{2\pi}\int_{-\phi_1}^{2\pi-\phi_1}\int_0^{\pi}\int_0^{\pi}\{\langle\tilde{G}_{12}(\theta_1,\theta_2,\phi_{\mathrm{d}},\mathscr{S}t)\rangle\}\sin^2\theta_1\sin^2\theta_2\cos\phi_{\mathrm{d}}\,\mathrm{d}\theta_2\,\mathrm{d}\theta_1\,\mathrm{d}\phi_{\mathrm{d}}\,\mathrm{d}\phi_1. \quad (7b)$$

By *analogy* with the Corcos (1964) model for the two-dimensional, homogeneous turbulent boundary layer wall pressure fluctuations on a flat plate, a separable, empirical model for $\tilde{G}_{12}$, is proposed, viz.,

$$\tilde{G}_{12}(\theta_1,\theta_2,\phi_d,\mathscr{S}t) = G_{11,n}(\mathscr{S}t)\Psi(\theta_1,\theta_2,\mathscr{S}t)\tilde{A}(\theta_1,\theta_2,\mathscr{S}t)B(\theta_1,\phi_d,\mathscr{S}t). \quad (8)$$

The first term is a normalization auto-power spectral density function defined at the streamwise location θ_n. The remaining functions are defined as follows:

$$\Psi(\theta_1,\theta_2,\mathscr{S}t) = \begin{cases}\dfrac{1}{G_{11,n}(\mathscr{S}t)}\dfrac{1}{(\theta_2-\theta_1)}\displaystyle\int_{\theta_1}^{\theta_2}G_{11}(\theta,\mathscr{S}t)\,\mathrm{d}\theta & \text{when } \theta_2\neq\theta_1,\\ \dfrac{G_{11}(\theta_1,\mathscr{S}t)}{G_{11,n}(\mathscr{S}t)} & \text{when } \theta_2=\theta_1,\end{cases} \quad (9)$$

$$\tilde{A}(\theta_1,\theta_2,\mathscr{S}t) = \frac{\tilde{G}_{12}(\theta_1,\theta_2,0,\mathscr{S}t)}{G_{11,n}(\mathscr{S}t)\,\Psi(\theta_1,\theta_2,\mathscr{S}t)}, \quad (10)$$

$$B(\theta_1,\phi_d,\mathscr{S}t) = \frac{\tilde{G}_{12}(\theta_1,\theta_1,\phi_d,\mathscr{S}t)}{G_{11,n}(\mathscr{S}t)\Psi(\theta_1,\theta_1,\mathscr{S}t)}. \quad (11)$$

The function Ψ is independent of ϕ because $G_{11}(\theta_1,\phi_1,\mathscr{S}t) = G_{11}(\theta_1,\phi_2,\mathscr{S}t) = G_{11}(\theta_1,\phi_3,\mathscr{S}t) = \cdots = G_{11}(\theta_1,\mathscr{S}t)$. It describes the variation of the average auto-power spectral density between two streamwise points relative to $G_{11,n}(\mathscr{S}t)$. The function $\tilde{A}$ accounts for the influence of θ separation with $\phi_d = 0$ on the cross-spectrum. It is complex because of

streamwise eddy convection. The function B accounts for the ϕ separation with $\theta_d = 0$. It is a real function because there is no mean convection of turbulent eddies in the ϕ-direction. The phase of $\tilde{G}_{12}$ is due solely to eddy convection in the streamwise direction. To further simplify Eq. (8), Eq. (11) is separated in its variables:

$$B(\theta_1, \phi_d, \mathscr{S}\ell) = B_1(\theta_1, \mathscr{S}\ell)B_2(\phi_d, \mathscr{S}\ell). \tag{12}$$

We note that $B_1(\theta_1,\mathscr{S}\ell)=B_1(\theta_2,\mathscr{S}\ell)$ because the magnitudes of $\tilde{G}_{12}$ and $\tilde{G}_{21}$ are equal. Eq. (7) then becomes

$$G_x(\mathscr{S}\ell) = \frac{\langle G_{11,n}(\mathscr{S}\ell)\rangle}{4\pi^2}\int_0^{2\pi}\int_{-\phi_1}^{2\pi-\phi_1}\int_0^{\pi}\int_0^{\pi}\{\langle(\theta_1,\theta_2,\mathscr{S}\ell)\rangle\langle\tilde{A}(\theta_1,\theta_2,\mathscr{S}\ell)\rangle \langle B_1(\theta_1,\mathscr{S}\ell)\rangle\langle B_2(\phi_d,\mathscr{S}\ell)\rangle \sin 2\theta_1 \sin 2\theta_2 \mathrm{d}\theta_2\,\mathrm{d}\theta_1\,\mathrm{d}\phi_d\,\mathrm{d}\phi_1, \tag{13a}$$

$$\begin{aligned} G_y(\mathscr{S}\ell) &= G_z(\mathscr{S}\ell) \\ &= \frac{\langle G_{11,n}(\mathscr{S}\ell)\rangle}{2\pi^2}\int_0^{2\pi}\int_{-\phi_1}^{2\pi-\phi_1}\int_0^{\pi}\int_0^{\pi}\langle\Psi(\theta_1,\theta_2,\mathscr{S}\ell)\rangle\langle\tilde{A}(\theta_1,\theta_2,\mathscr{S}\ell)\rangle \\ &\quad \langle B_1(\theta_1,\mathscr{S}\ell)\rangle\langle B_2(\phi_d,\mathscr{S}\ell)\rangle \sin^2\theta_1 \sin^2\theta_2 \cos\phi_d \\ &\quad \times \mathrm{d}\theta_2\,\mathrm{d}\theta_1\,\mathrm{d}\phi_d\,\mathrm{d}\phi_1. \end{aligned} \tag{13b}$$

By defining

$$\Lambda_1(\mathscr{S}\ell) = \frac{1}{2\pi}\int_0^{2\pi}\int_{-\phi_1}^{2\pi-\phi_1}\langle B_2(\phi_d,\mathscr{S}\ell)\rangle\,\mathrm{d}\phi_d\,\mathrm{d}\phi_1, \tag{14}$$

$$\Lambda_2(\mathscr{S}\ell) = \frac{1}{\sqrt{2}\pi}\int_0^{2\pi}\int_{-\phi_1}^{2\pi-\phi_1}\langle B_2(\phi_d,\mathscr{S}\ell)\rangle\cos\phi_d\,\mathrm{d}\phi_d\,\mathrm{d}\phi_1, \tag{15}$$

$$\Lambda_3(\mathscr{S}\ell) = \frac{1}{2\pi}\int_0^{\pi}\int_0^{\pi}\langle\Psi(\theta_1,\theta_2,\mathscr{S}\ell)\rangle\langle\tilde{A}(\theta_1,\theta_2,\mathscr{S}\ell)\rangle\langle B_1(\theta_1,\mathscr{S}\ell)\rangle\sin 2\theta_1 \sin 2\theta_2\,\mathrm{d}\theta_2\,\mathrm{d}\theta_1, \tag{16}$$

$$\Lambda_4(\mathscr{S}\ell) = \frac{1}{\sqrt{2}\pi}\int_0^{\pi}\int_0^{\pi}\langle\Psi(\theta_1,\theta_2,\mathscr{S}\ell)\rangle\langle\tilde{A}(\theta_1,\theta_2,\mathscr{S}\ell)\rangle\langle B_1(\theta_1,\mathscr{S}\ell)\rangle\sin^2\theta_1 \sin^2\theta_2\,\mathrm{d}\theta_2\,\mathrm{d}\theta_1. \tag{17}$$

Eq. (13) becomes

$$G_x(\mathscr{S}\ell) = \langle G_{11,n}(\mathscr{S}\ell)\rangle\Lambda_1(\mathscr{S}\ell)\Lambda_3(\mathscr{S}\ell), \tag{18a}$$

$$G_y(\mathscr{S}\ell) = G_z(\mathscr{S}\ell) = \langle G_{11,n}(\mathscr{S}\ell)\rangle\Lambda_2(\mathscr{S}\ell)\Lambda_4(\mathscr{S}\ell). \tag{18b}$$

Here, $\Lambda_1(\mathscr{S}\ell)$ and $\Lambda_2(\mathscr{S}\ell)$ may be termed the angular correlation area in the ϕ-direction for the auto-power spectra of the unsteady drag and lift coefficient, respectively. Likewise, $\Lambda_3(\mathscr{S}\ell)$ and $\Lambda_4(\mathscr{S}\ell)$ are the angular correlation areas for the drag and lift spectra in the θ-direction. The next task is to choose $G_{11,n}(\mathscr{S}\ell)$, to introduce models for $\Psi(\theta_1,\theta_2,\mathscr{S}\ell)$, $\tilde{A}(\theta_1,\theta_2,St)$, $B_1(\theta_1,\mathscr{S}\ell)$, and $B_2(\phi_d,\mathscr{S}\ell)$, and to calculate the angular correlation areas $\Lambda_i(\mathscr{S}\ell)$, $i=1$–4. These models are based on measured statistics of the surface pressure fluctuations on a sphere in steady, uniform flow.

3. Surface pressure measurements

The surface pressure fluctuations on a sphere were measured in a low-noise, open-channel wind tunnel, which was operated inside an anechoic chamber. The test-section is 45.72 cm square by 1.5 m long. Upstream of the test section is an 11:1 contraction section and turbulence management screens. Downstream is a 2.6 m long, 7° diffuser. Details of the wind tunnel and its performance characteristics can be found in Wang (1999).

Two hemispheres, machined from 4-mm-thick plastic marine buoyancy balls were secured together with a thin tape to make the 15.24-cm-diameter test sphere. Pressure transducers could be located in any of the 120, 0.234 cm diameter holes drilled into the sphere surface. Modelling clay was used to fill holes not occupied by a transducer. The adhesive tape strips were located far away from measurement points to avoid possible signal contamination from their minimal influence on the local flow. As sketched in Fig. 2, the sphere was rigidly mounted on a 30.48 cm long steel sting, which was threaded onto a vertical steel tube of elliptical cross section. This tube was anchored to the concrete floor of the anechoic chamber. The sphere was centered in the square test section.

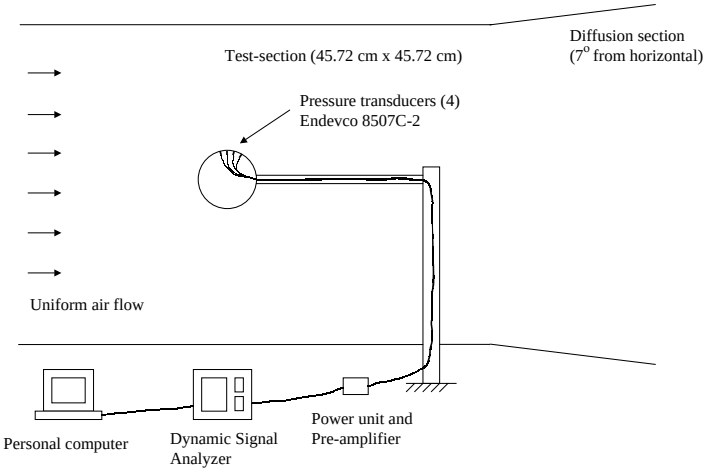

Fig. 2. Schematic of the wind tunnel test section (side view).

Prior to making surface pressure measurements, velocity field surveys were performed in the absence of the test sphere at $U_0 = 1.75$, 2.52, and 3.12 m/s, which correspond to Re = 17,800, 25,600, 31,700, respectively. Hot-wire measurements were made in a plane normal to the flow direction and passing the virtual forward stagnation point of the sphere. For all speeds, the variation of the local mean velocity across the test section was less than $\pm 2\%$. The streamwise component of free-stream turbulence intensity was less than 0.5%. The flow field around the sphere was observed using smoke-wire flow visualization techniques. For the Re range noted above, the flow separated from the sphere at approximately 80° from the forward stagnation point and the near wake was turbulent, so the flow was determined to be sub-critical.

The test section background noise was measured with a Brüel and Kjæslit tube to determine the pressure transducer signal-to-background noise ratio. The slit tube, mounted in the test section, attenuates nonacoustic, flow-induced pressure fluctuations on the microphone itself. The measured signal-to-noise ratios were 6 dB or higher, except for $40 < f < 60$ Hz, which was affected by the wind tunnel blower noise. The spectra of the surface pressure fluctuations were observed to decay rapidly for $f > 60$ Hz, so the surface pressure measurements were confined to $1 < f < 40$ Hz.

Tunnel blockage or flow confinement may possibly affect the correlation measurements on bluff bodies, e.g., Blackburn (1994). Maskell (1963) gives a formula for estimating the effect of tunnel blockage on the steady-state drag coefficient of bluff bodies in steady flow:

$$(C_d - C_{dc})/C_d \cong \alpha(A_s/A_t)C_d, \tag{19}$$

where C_d is the drag coefficient in the wind tunnel, C_{dc} is the correct drag coefficient in an infinite medium, $\alpha = 2.5$ for a symmetrical three-dimensional bluff body, A_s is the frontal area of the body, and A_t is the test section area. For this investigation, $(C_d - C_{dc})/C_d \cong 0.087$. Although this calculation is for the mean drag coefficient, the unsteady drag is a small perturbation about the mean, and directly related to the wall pressure statistics. We assume therefore that the tunnel blockage has a similar effect on the unsteady pressure measurements, i.e., they should be within 9% of unbounded flow measurements.

The unsteady pressures were measured using four 0.234 cm diameter Endevco model 8507C-2 piezoresistive pressure transducers, which have flat frequency response from DC to 14 kHz. Batteries were used as the power supply to avoid the electromagnetic interference of the 60 Hz power line. Phase calibrations between all sensor pairs were performed using a standing-wave tube. The phase varied within $\pm 2°$ for $f < 600$ Hz.

Spectral data were acquired using a dynamic signal analyzer. It was set up to use 1000 ensemble averages, a uniform window, 0–800 Hz frequency range, and 800 lines of resolution, meaning an effective analysis bandwidth of 1 Hz. The random error in spectral amplitude is inversely proportional to the square root of the number of spectral averages, e.g., Bendat and Piersol (2000). The random error for these tests is ± 0.1 dB. The uniform window was chosen to avoid distortion at very low frequencies.

4. Measurement results and semi-empirical model

4.1. Auto-power spectral density G_{11}

Fig. 3 shows $G_{11}(f)$ for Re = 31,700 and $\theta = 0-163^\circ$. The farthest streamwise angular location is limited to $\theta = 163^\circ$ because of the supporting sting at the downstream side of the sphere. The low-mode (Kim and Durbin, 1988) vortex shedding frequency under this condition is 4 Hz. The shedding frequency appears in the spectrum of wall pressure fluctuations, particularly at the separation point ($\theta = 80^\circ$). The spectra measured in the laminar flow region ($\theta < 80^\circ$) are lower in level than those measured farther downstream in the turbulent regions; therefore, the subsequent modelling

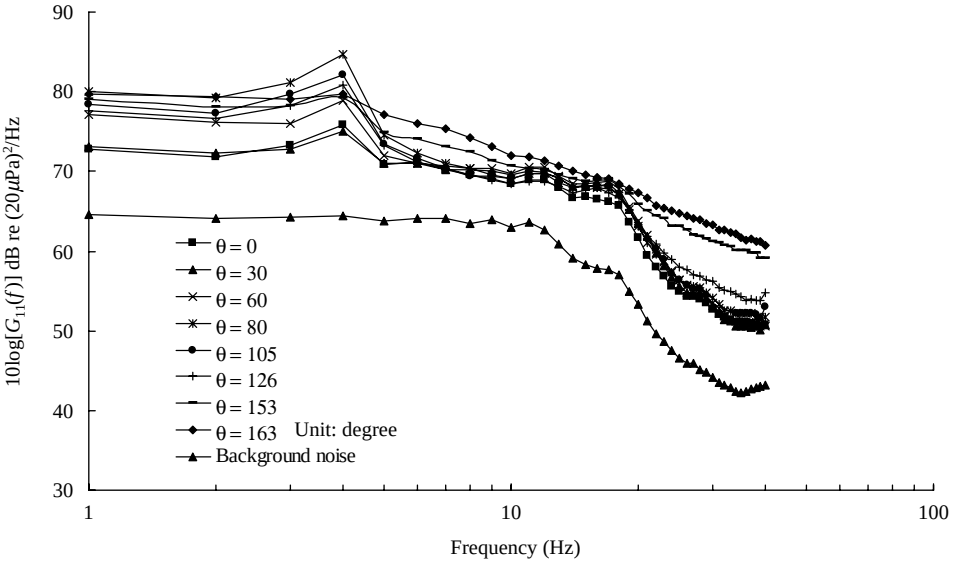

Fig. 3. Auto-power spectral densities of the surface pressure fluctuations at different streamwise locations for $U_0 = 3.12$ m/s (Re = 31,700).

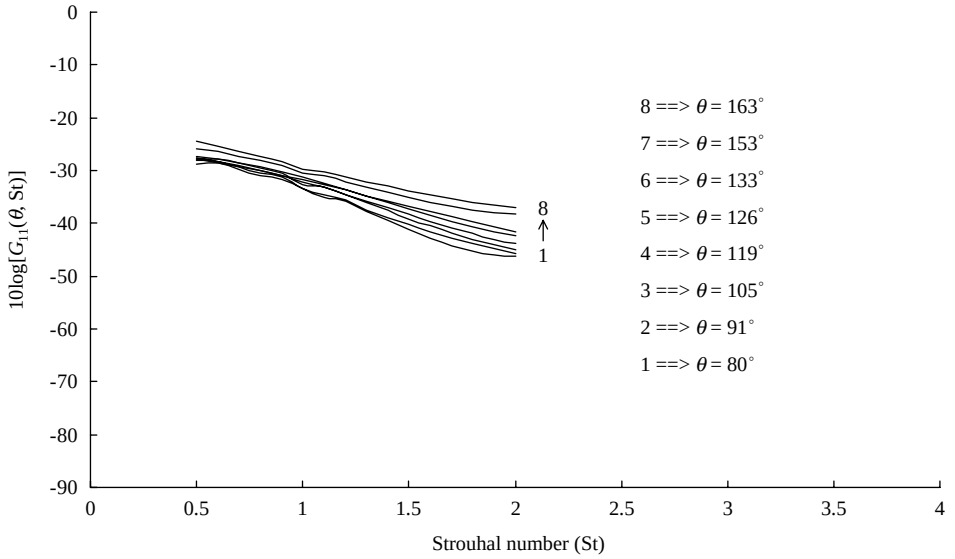

Fig. 4. Fitting curves of the dimensionless auto-power spectral densities of the surface pressure fluctuations at different θ locations in the turbulent region.

Table 1
Coefficients used in the empirical models for the auto- and cross-power spectral density functions

$\mathscr{S}\ell$	0.50	0.60	0.70	0.80	0.90	1.00	1.10	1.20	1.3	1.4	1.5	1.6	1.7	1.8	1.9	2
g_3	3.56	3.17	3.03	2.61	2.43	2.17	1.93	1.64	1.44	1.72	2.02	2.29	2.51	2.89	2.43	1.89
g_2	−20.88	−18.48	−17.95	−15.51	−14.24	−12.74	−11.23	−8.88	−7.48	−8.98	−10.46	−11.73	−12.55	−12.47	−10.85	−6.85
g_1	40.56	35.57	35.28	30.84	27.99	25.28	22.81	16.99	14.27	17.13	19.71	21.65	22.5	21.37	16.99	7.72
g_0	−24.06	−20.33	−20.66	−18.13	−15.97	−14.89	−13.70	−9.15	−7.81	−9.817	−11.49	−12.58	−12.82	−11.63	−8.21	−1.49
a_2	−3.42	−3.50	−3.40	−3.40	−3.30	−3.20	−3.00	−3.00	−2.90	−2.80	−2.80	−2.70	−2.30	−2.30	−2.30	−2.20
a_1	0.84	1.10	1.30	1.30	1.20	0.94	0.67	0.55	0.29	0.05	−0.15	−0.30	−0.80	−0.80	−0.70	−0.60
b_2	0.010	0.009	0.006	0.001	−0.003	−0.009	−0.014	−0.019	−0.023	−0.027	−0.030	−0.032	−0.032	−0.031	−0.028	−0.023
b_1	−0.093	−0.096	−0.100	−0.103	−0.107	−0.113	−0.119	−0.128	−0.138	−0.148	−0.160	−0.172	−0.185	−0.198	−0.211	−0.225
e_3	1.59	1.51	1.51	1.58	1.74	1.99	2.33	2.77	3.31	3.96	4.73	5.6	6.6	7.73	8.98	10.37
e_2	−2.40	−2.87	−3.09	−3.31	−3.57	−3.90	−4.31	−4.84	−5.52	−6.37	−7.42	−8.69	−10.22	−12.02	−14.13	−16.57
e_1	0.47	0.84	1.09	1.24	1.32	1.36	1.40	1.44	1.54	1.7	1.97	2.37	2.93	3.68	4.65	5.86

concentrates on the measurement results in the turbulent region, above the low-mode shedding frequency. We note there is no evidence of the high-mode shear layer instability frequency in these data. This is because high-mode frequency must be detected with sensors placed in the wake flow. The nondimensionalized $G_{11}(\mathscr{S}\ell)$ are given in Fig. 4, which are the spectra averaged from three separate test runs. The spectrum at $\theta = 80^\circ$ is chosen as the normalization spectrum $G_{11,n}(\mathscr{S}\ell)$ because the separation point on the sphere's surface represents a well-defined, characteristic location. Exponential functions of third-order polynomials are used to fit $G_{11,n}(\mathscr{S}\ell)$ and $G_{11}(\theta, \mathscr{S}\ell)$ with least mean-square errors:

$$G_{11,n}(\mathscr{S}\ell) \approx \exp(2.70\mathscr{S}\ell^3 - 10.44\mathscr{S}\ell^2 + 9.26\mathscr{S}\ell - 8.97), \tag{20}$$

$$G_{11}(q, \mathscr{S}\ell) = (g_3\theta^3 + g_2\theta^2 + g_1\theta + g_0)\exp(0.86\mathscr{S}\ell^3 - 3.08\mathscr{S}\ell^2 + 0.82\mathscr{S}\ell - 6.85). \tag{21}$$

The coefficients g_0–g_3 are functions of $\mathscr{S}\ell$ and are given in Table 1. The unit of θ is radian.

The angle-averaged auto-power spectral density function, $\Psi(\theta_1, \theta_2, \mathscr{S}\ell)$ can be obtained using Eq. (9) and expressed as follows:

$$\begin{aligned}\Psi(\theta_1, \theta_2, \mathscr{S}\ell) = {} & \{0.25g_3(\theta_2^3 + \theta_2^2\theta_1 + \theta_2\theta_1^2 + \theta_1^3) + 0.33g_2(\theta_2^2 + \theta_2\theta_1 + \theta_1^2) + 0.5g_1(\theta_2 + \theta_1) + g_0\} \\ & \times \exp(-1.84\mathscr{S}\ell^3 + 7.36\mathscr{S}\ell^2 - 8.44\mathscr{S}\ell + 2.12),\end{aligned} \tag{22}$$

where $\theta_2, \theta_1 \geqslant 80^\circ$.

4.2. Cross-power spectral density $\tilde{G}_{12}$

It is necessary to verify the two major assumptions made in Section 2. The first is the homogeneity of $\tilde{G}_{12}$ in the ϕ-direction, i.e., to verify Eq. (6). The second is the separability of $\tilde{G}_{12}$ into the streamwise ($\tilde{A}$) and circumferential (B) functions, i.e., to verify Eq. (8). The homogeneity assumption is verified by fixing the measurement locations on the sphere's surface while rotating the sphere about the x-axis as to the change of ϕ_r. Several different combinations of measurement locations (θ_1, ϕ_1) and (θ_2, ϕ_2) were tested to confirm this assumption. Fig. 5 shows one combination for rotation angles of 0°, 45°, and 75°. All other tests, which included changes of θ_1, ϕ_1, θ_2, ϕ_2, ϕ_r, and Re, show similar results. Therefore, $\tilde{G}_{12}$ is proven to be homogeneous in the circumferential direction. Also, the phase of $\tilde{G}_{12}$ is seen to be very nearly zero confirming the assumption in Section 2 that the function B is real.

The separability assumption is verified using three-point cross-power spectral measurements at locations (θ_1, ϕ_1), (θ_{II}, ϕ_{II}), $(\theta_{III}, \phi_{III})$, with $\phi_I = \phi_{II}$ and $\theta_{II} = \theta_{III}$. The cross-spectral densities are nondimensionalized by the product of $G_{11,n}(\mathscr{S}\ell)$ and $\Psi(\theta_1,\theta_2,\mathscr{S}\ell)$. The dimensionless cross-spectrum between points I and II represents the $\tilde{A}$ function, and that between points II and III represents the B function. Within a tolerance of 2 dB, Fig. 6 shows that the magnitude of the directly measured cross-spectrum agrees with that calculated from the separable assumption. The phases determined by the two methods are also in excellent agreement. Other tests for different locations and Re show very similar trends. The separable assumption is thus proven to be viable.

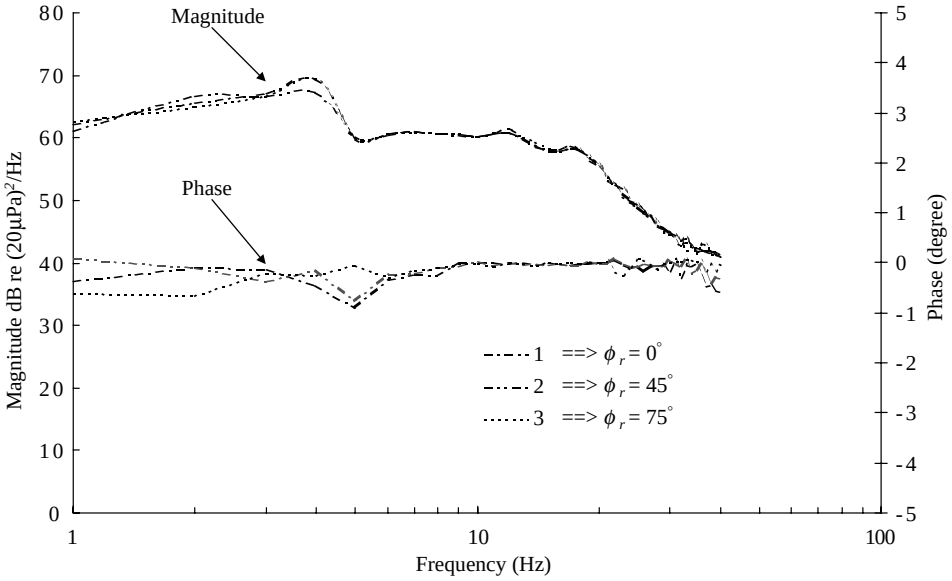

Fig. 5. Comparison of the magnitudes and phases of $\tilde{G}_{12}(\theta_1, \phi_1, \theta_2, \phi_2, f)$ vs. f for $(\theta_1, \phi_1) = (112^\circ, 0^\circ)$, $(\theta_2, \phi_2) = (112^\circ, 55^\circ)$, and $U_0 = 3.12\,\text{m/s}$ (Re = 31,700).

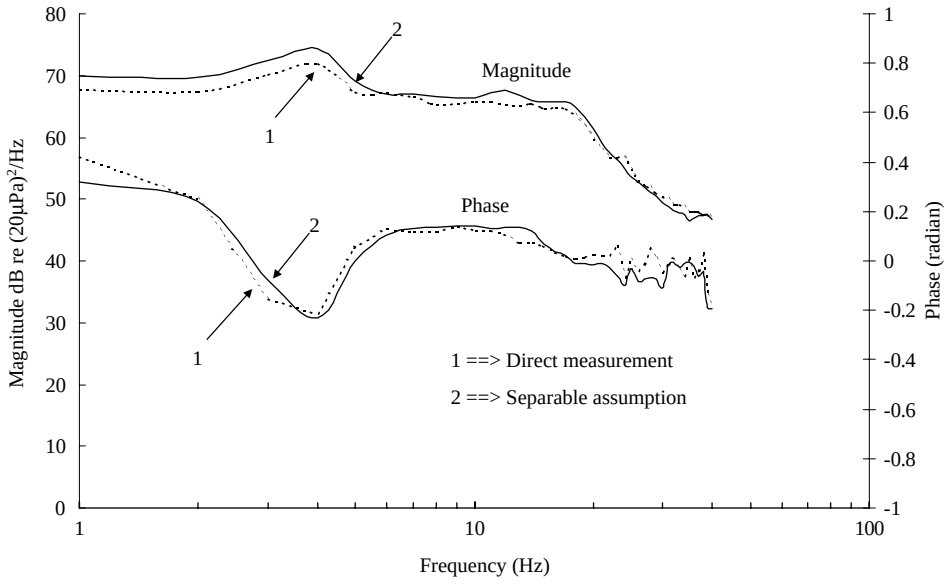

Fig. 6. Comparison of the magnitudes and phases of cross-power spectral densities with $(\theta_\text{I}, \phi_\text{I}) = (91^\circ, 0^\circ)$, $(\theta_\text{II}, \phi_\text{II}) = (112^\circ, 0^\circ)$, and $(\theta_\text{III}, \phi_\text{III}) = (112^\circ, 55^\circ)$, at $U_0 = 3.12\,\text{m/s}$ (Re = 31,700).

The $\tilde{A}$ function is modelled as follows:

$$|\tilde{A}(\theta_1, \theta_2, \mathscr{S}\ell| = \{0.23(\theta_1)^3 - 1.52(\theta_1)^2 + 2.46\theta_1\}\exp[a_2|\theta_d|^2 + a_1|\theta_d|] \times \exp[0.09\mathscr{S}\ell^3 - 0.51\mathscr{S}\ell^2 + 0.41\mathscr{S}\ell - 0.12], \tag{23}$$

where coefficients a_1 and a_2 are listed in Table 1. Fig. 7 shows the fitting curves of $|\tilde{A}|$ for $\theta_1 = 91^\circ$. For fixed separation ($\theta_d = \theta_2 - \theta_1$), this model predicts an exponential decrease in $|\tilde{A}|$ with increasing $\mathscr{S}\ell$. This is because the fluctuations at high frequencies are associated with small-scale turbulent eddies, which decay more rapidly than large-scale eddies for

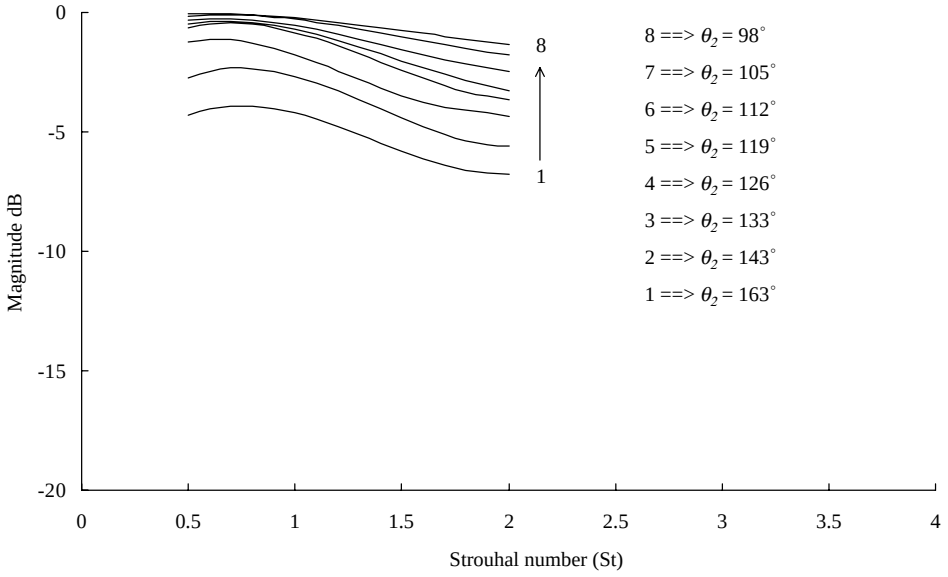

Fig. 7. Fitting curves of $|\tilde{A}(St)|$ for $\theta_1 = 91^\circ$ and different θ_2.

any given θ_d. The function $|\tilde{A}|$ also decreases with increasing θ_d because the turbulent eddies lose coherence at larger separation distances. The dynamic wall pressure field on a sphere is clearly nonhomogeneous in the streamwise direction.

Modelling the phase of $\tilde{A}$, which is of maximum order ± 0.3 rad, is difficult. Fortunately, the effect of the phase is negligible on the estimation of the unsteady force because only the real parts of the cross-spectra of the unsteady surface pressures contribute, e.g., Wang (1999). Noting that $\text{Real}\{\tilde{A}\} = |\tilde{A}|\cos(\pm 0.3) = \pm 0.96|\tilde{A}|$, Neglecting the phase variations results in a ± 0.2 dB error in the estimation of the unsteady force.

The real-valued B function of Eq. (12) is separated into B_1 and B_2 functions. The empirical models for these two functions are:

$$B_2(\phi_d, \mathscr{S}t) = \exp(b_2|\phi_d|^2 + b_1|\phi_d|)\exp(0.06\mathscr{S}t^3 - 0.34\mathscr{S}t^2 + 0.30\mathscr{S}t - 0.1), \tag{24}$$

$$B_1(\theta_1, \mathscr{S}t) = e_3(\theta_1 - 1.396)^3 + e_2(\theta_1 - 1.396)^2 + e_1(\theta_1 - 1.396) + 1, \tag{25}$$

where the Strouhal number-dependent constants are given in Table 1.

4.3. Error analysis

In this experiment, the systematic error (bias error) is minimized by regularly calibrating the transducers. The calibrations show less than 0.5% variation during the course of the measurements. As noted in Section 3, the random error in measured spectral data is estimated to be ± 0.1 dB.

Besides the measurement errors, uncertainty is introduced when the dimensional data are nondimensionalized and averaged over different flow speeds. Additional errors are introduced by the least mean-square fitting of the data curves, each of which produces a small fractional and cumulative error. Because each curve fitting is different, the curve-fitting errors have to be discussed individually.

Nondimensionalization of $G_{11,n}(\mathscr{S}t)$ introduces ± 1.5 dB uncertainty at $\theta = 80^\circ$ according to the average scatter among the spectra of the three test Reynolds numbers. The curve fitting of $G_{11,n}(\mathscr{S}t)$ vs. $\mathscr{S}t$ introduces an estimated ± 0.1 dB (or $\pm 3\%$) error. The overall estimation error for the model of $G_{11,n}(\mathscr{S}t)$ is thus ± 1.6 dB.

The curve fitting of $G_{11}(\theta, \mathscr{S}t)$ vs. $\mathscr{S}t$ introduces an estimated ± 0.1 dB (or $\pm 3\%$) error, while that of $G_{11}(\theta, \mathscr{S}t)$ vs. θ also introduces an estimated ± 0.1 dB (or $\pm 3\%$) error. The overall error for the model of $G_{11}(\theta, \mathscr{S}t)$ is ± 0.3 dB (or $\pm 6\%$). As a result, the function $\Psi(\theta_1, \theta_2, \mathscr{S}t)$, calculated using Eq. (9), has ± 1.9 dB uncertainty, of which ± 1.6 dB is from estimation during the nondimensionalization process and ± 0.3 dB from curve-fitting processes.

The curve fitting of $|\tilde{A}(\theta_1, \theta_d, St)|$ vs. θ_d and $\mathscr{S}\ell$ each introduces an estimated ± 0.1 dB (or $\pm 3\%$) error, while that of $|\tilde{A}(\theta_1, \theta_d, St)|$ vs. θ_1 introduce an estimated ± 0.1 dB (or $\pm 2\%$) error. The overall estimation error for the model of $|\tilde{A}(\theta_1, \theta_d, St)|$ is thus ± 0.4 dB (or $\pm 8\%$). The curve fitting of $B_2(\phi_d, \mathscr{S}\ell)$ vs. $\mathscr{S}\ell$ and ϕ_d each introduces an estimated ± 0.1 dB (or $\pm 3\%$) error. The curve fitting of $B_1(\theta_1, \mathscr{S}\ell)$ introduces an estimated ± 0.1 dB (or $\pm 3\%$) error. The overall estimation error for the model of $B(\theta_1, \phi_d, \mathscr{S}\ell)$ is ± 0.4 dB (or $\pm 9\%$).

4.4. Unsteady force calculation

The nondimensional angular correlation areas Λ_1–Λ_4 can now be calculated from Eqs. (14)–(17) and are shown in Fig. 8. One should not mistake Λ_1–Λ_4 as the correlation functions of surface pressure fluctuations. Those are implied in $|\tilde{A}|$ for the θ-direction, and in B_2 for the ϕ-direction. The functions Λ_1–Λ_4 are used in Eq. (18) to obtain the spectral densities of the unsteady drag and lift forces.

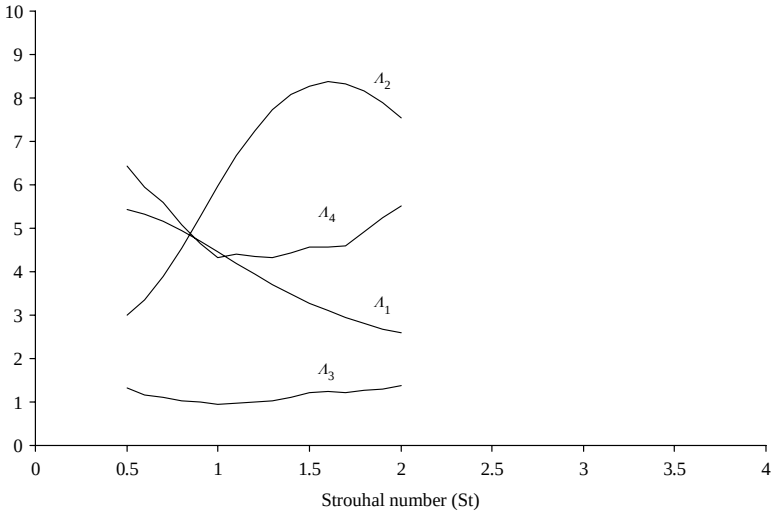

Fig. 8. Dimensionless angular correlation areas for the ϕ and θ directions.

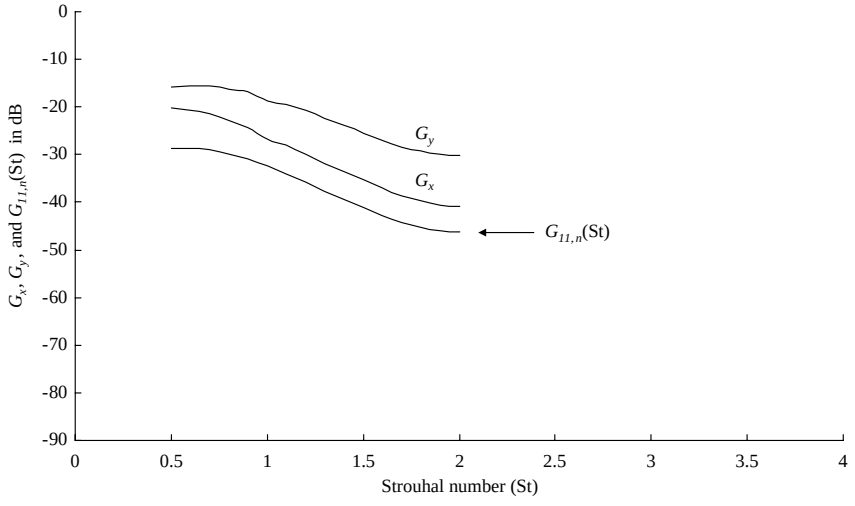

Fig. 9. Dimensionless power spectral densities of the unsteady lift and drag forces compared with $G_{11,n}(\mathscr{S}\ell)$.

The estimation errors for $\Lambda_1-\Lambda_4$ can be calculated from the previous error analysis. Λ_1 and Λ_2 each has an estimated $\pm 6\%$ error, while Λ_3 and Λ_4 each has an estimated $\pm 27\%$ error, which includes an estimated $\pm 4\%$ error for neglecting the phases of the $\tilde{A}$ function.

There is no simple, explicit formula derived here for $\Lambda_1-\Lambda_4$ because the fluctuating flow around the sphere is statistically nonhomogeneous in the streamwise direction, meaning that $\tilde{A}$ and B include coefficients that depend on Strouhal number (Table 1). The empirical model, however, is directly applied because the integrals of Eqs. (14)–(17) are easy to evaluate numerically.

Fig. 9 presents the computations from Eq. (18). The predicted unsteady lift force is from 4 to 10 dB higher than the predicted unsteady drag force. Both spectral densities show a $\mathscr{S}t^0$ at low $\mathscr{S}t$, and a $\mathscr{S}t^{-3}$ dependence at high values of $\mathscr{S}t$. Fig. 9 also includes a plot of the characteristic spectral density $G_{11,n}(\mathscr{S}t)$. Comparison of this with the other curves in the figure shows that the shape of the Λ_1–Λ_4 curves of Fig. 8 is insignificant on the force calculations in a dB scale. For practical purposes, the Strouhal number dependence of the correlation areas can be neglected and their values replaced by the mean values $\bar{\Lambda}_i$ ($i=1-4$) determined by integration of the curves in Fig. 8. We find: $\bar{\Lambda}_1=4.0$; $\bar{\Lambda}_2=6.0$; $\bar{\Lambda}_3=1.0$; $\bar{\Lambda}_4=5.0$. The estimated error for the unsteady lift and drag forces is about ± 3.3 dB. The function $G_{11,n}(\mathscr{S}t)$ contributes ± 1.6 dB, while the error propagation from the curve fitting is ± 1.7 dB.

5. Tow tank experiment

An experiment is now described where the flow-induced unsteady side force and drag force are measured independently of each other on towed spheres in a basin of water.

5.1. Experimental setup

The tow tank and supporting apparatus are sketched in Fig. 10. The fiberglass tank is 25.4 cm wide, 25.4 cm deep and 9.2 m long. The towed sphere moves along the centerline of the tank, suspended by four fishing lines tied to aluminum rods that are bolted to the bottom of a trolley. A computer-controlled linear micro-stepping motor drives a loop of plastic-coated, braided steel cable that moves the trolley along the length of a rail. The tank is supported on resilient

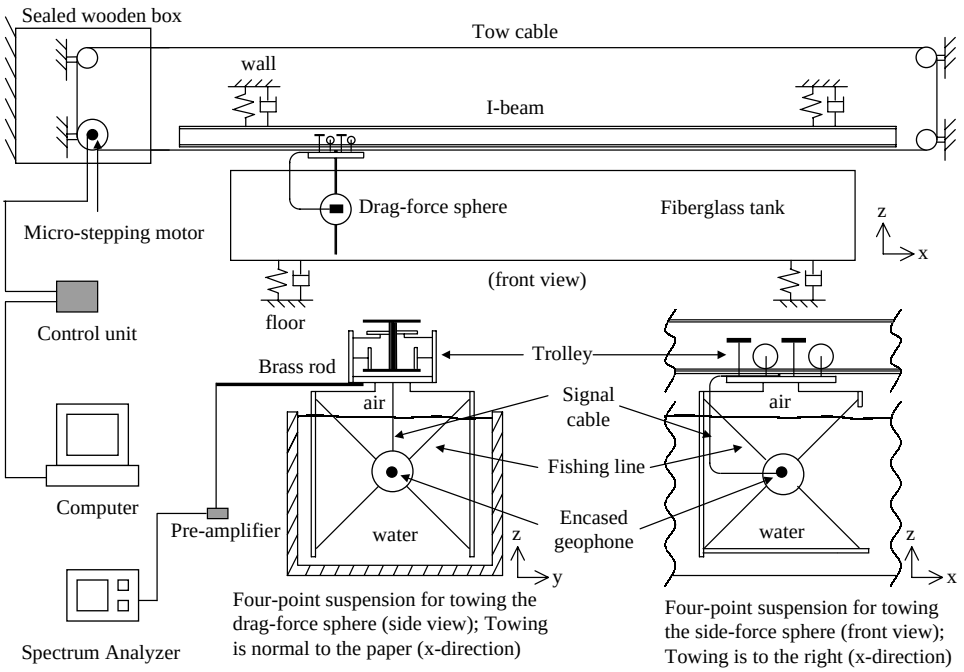

Fig. 10. Quiet tow tank facility and supporting apparatus.

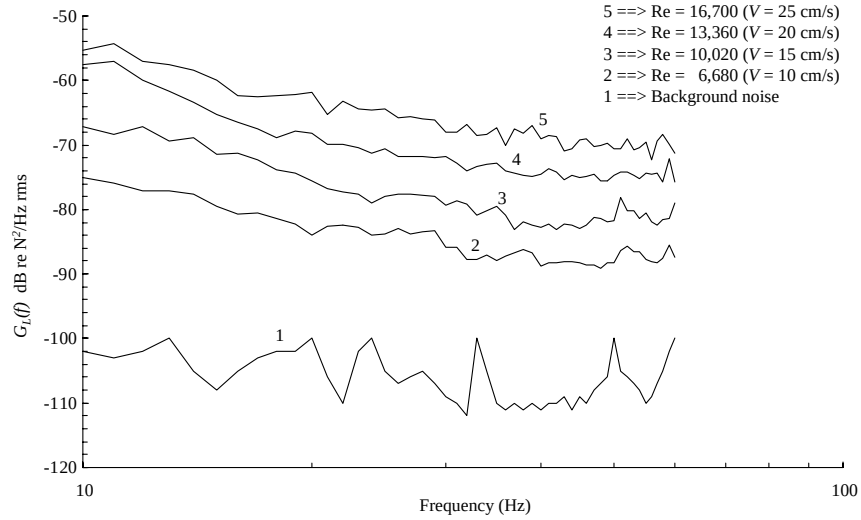

Fig. 11. Unsteady side-force spectra measured at various speeds on the towed side-force sphere.

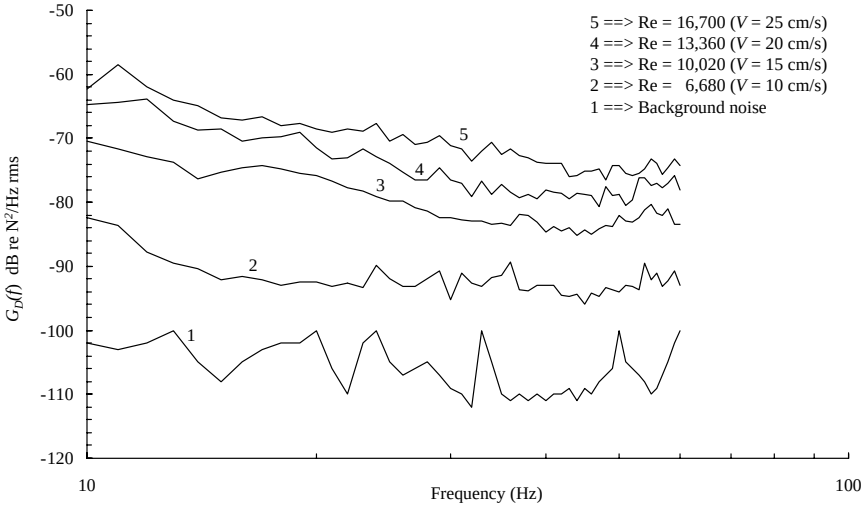

Fig. 12. Unsteady drag-force spectra measured at various speeds on the towed drag-force sphere.

mounts to reduce any vibration transmission from the laboratory floor. The drive motor is mounted in an enclosure to minimize the effect of motor noise.

Two spherical models are made, respectively, for measuring the unsteady drag and side forces. Each 7.62-cm-diameter model is made from a volume mixture of 14 parts polystyrene micro-balloons to 3 parts epoxy resin cast in a spherical mold. This combination of materials results in a neutrally buoyant sphere. A Geospace Corp., GS20-DH7 geophone is encased at the center of the spherical mold and oriented in the appropriate direction for sensing the unsteady velocity due to the unsteady drag or side force. The sensitivity of these models to flow-induced motion (and also acoustic disturbances) is maximized when the models are neutrally buoyant. The sensors are calibrated with respect to a standard accelerometer both in air and in water by using an electromagnetic shaker. Added mass effects are accounted for.

The four-point suspension of the side-force sphere limits the motion of the sphere to the y-direction, while the suspension of the drag-force sphere limits the motion to only the x-direction. The signal cable exits the sphere at the rearward stagnation point to avoid any influence from the wake of the signal cable.

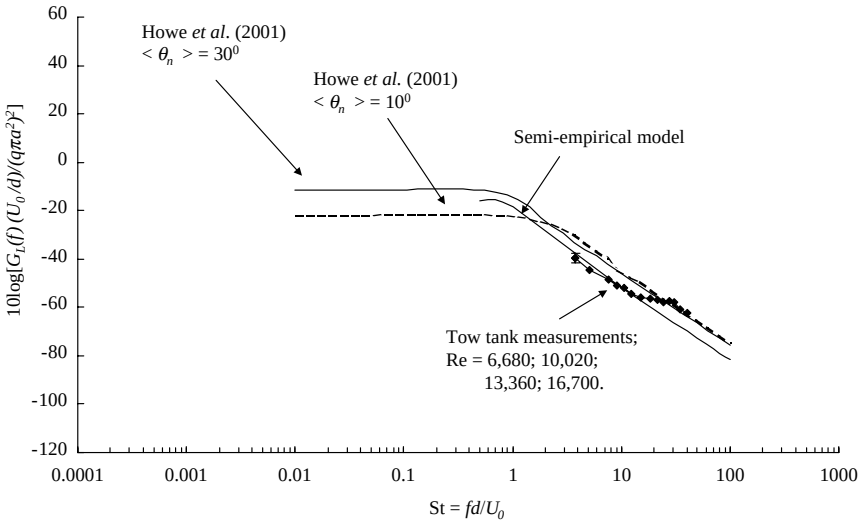

Fig. 13. Dimensionless power spectra of the unsteady side force. The error bar at $\mathscr{S}\ell = 4$ represents the maximum spread of the data.

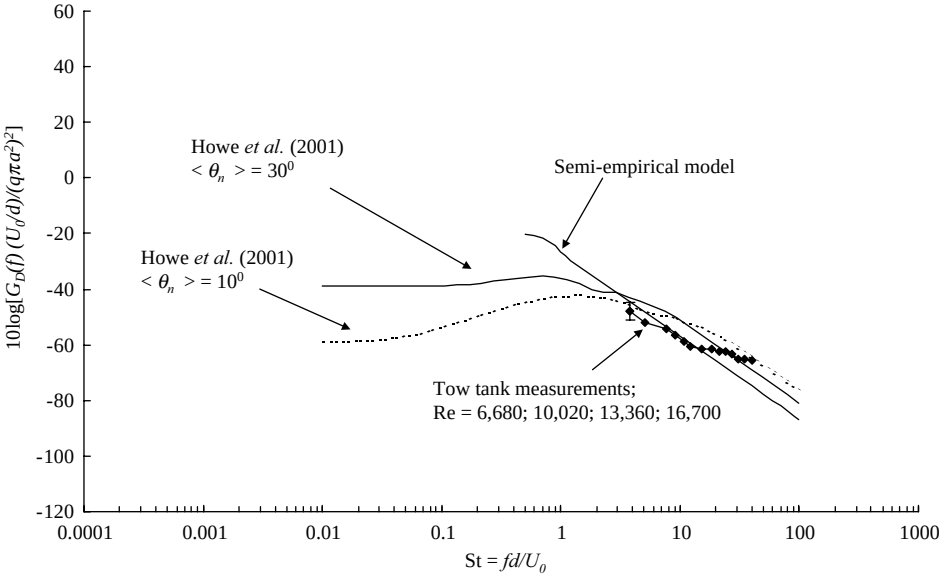

Fig. 14. Dimensionless power spectra of the unsteady drag force. The error bar at $\mathscr{S}\ell = 4$ represents the maximum spread of the data.

The spheres are towed at four different speeds: 10, 15, 20 and 25 cm/s, corresponding to $6680 \leqslant \mathrm{Re} \leqslant 16{,}700$. The geophone signal cable is connected to a 40 dB pre-amplifier and to a spectrum analyzer. Because of the limited time available for each tow run, the data from several runs at the same towing speed are averaged to achieve a total of 100 averages. The random error in the present spectral data is 0.4 dB.

5.2. Results

The measured power spectral densities of the side and drag forces [$G_L(f)$ and $G_D(f)$, respectively] are shown in Figs. 11 and 12. The background noise force, measured when the mechanical components were functioning but no flow, was 10 dB or more lower than all the signals. The measured and predicted lift and drag coefficient spectral densities are shown in Figs. 13 and 14, respectively. The levels of $G_L(f)$ are 3–7 dB higher than those of $G_D(f)$. This is in agreement

with the predictions from the empirical model presented here, and with the analytical model of Howe et al. (2001). Aside from the ± 2 dB scatter due to random errors, the results of the tow tank measurement compare rather well with the high-Strouhal number predictions. It is difficult to judge the quantitative differences of the predictions based on the two models. For $\mathscr{S}t < 1$, the model of Howe et al. (2001) depends on the mean orientations of shed vortices, $\langle \theta_n \rangle$, for which no direct experimental information is available. Although the empirical model is based on direct wall pressure statistics, it depends on the separable assumption and on the curve-fitting processes of the model functions. The separable assumption tends to overestimate the cross-power spectral densities at low Strouhal numbers, and the error propagation from curve fitting may be as high as ± 3.3 dB. Thus, within the accuracy of either model, the comparisons shown in Figs. 13 and 14 are considered quite good. This further suggests that the extrapolation of the empirical model curves using $\mathscr{S}t^{-3}$ to higher values of $\mathscr{S}t$ is valid.

6. Conclusions

A rigid sphere subjected to steady uniform flow experiences unsteady lift and drag. The high-frequency spectra of these unsteady forces are determined by an empirical model based on measured wall pressure statistics, and by direct tow tank measurement. The unsteady force is computed from the integral of the wall pressure fluctuations generated in the turbulent flow regimes over the sphere's surface. This is a direct consequence of the separated boundary layer and the formation of vorticity in the near wake. The surface pressure fluctuations are found to be statistically homogeneous in the circumferential direction, and nonhomogeneous in the streamwise direction. For Strouhal numbers above the low-mode shedding frequency, the auto-power spectral density (and the magnitude of the cross-spectrum) of the surface pressure fluctuations is broadband and decays exponentially with Strouhal number. The magnitude of the spatial cross-spectrum decays more rapidly for circumferential separations than it does for streamwise separations. This is because the turbulent energy is convecting in the streamwise direction causing the eddies to retain coherence over longer streamwise distances than they do in the circumferential direction. A separation of variables assumption is invoked on the cross-spectral densities, which turns out to be a good engineering approximation. Because of the nonhomogeneous nature of the streamwise wall pressure field, the separable form must, however, include a function that describes the cross-spectrum dependence on the reference location.

The empirical model predicts the auto-spectral densities of both the unsteady lift and the unsteady drag. Both are shown to be $\mathscr{S}t^0$ dependent for $\mathscr{S}t < 1$ and $\mathscr{S}t^{-3}$ dependent for $1 \leqslant \mathscr{S}t \leqslant 100$. The model predicts that the unsteady lift force levels are 3–7 dB higher than those of the unsteady drag force. This is in very good agreement with the spectral data obtained in the tow tank experiments, and with the predictions based on the ring vortex model of Howe et al. (2001). The Howe et al. model hypothesizes that the dominant source of unsteady force is the nascent vortex ring of the low-mode shedding process. The random orientation of successively shed vortex rings produces the nondiscrete broadband features of the high-frequency force fluctuation. Because of the strong agreement among the actual force data, the predictions with the empirical model, and the predictions with the ring vortex model, it is concluded that the turbulent wall pressure field created over $80^\circ \leqslant \theta \leqslant 180^\circ$ is very likely the result of the low-mode vortex shedding process, which of course, is trigged by the boundary layer separation at $\theta = 80^\circ$. Either model can be used with confidence to predict the flow-induced self-noise on underwater inertial acoustic sensors, as is done in Wang (1999).

Acknowledgements

This work was supported by ONR Code 321SS, under grant numbers N00014-96-1-0005, N00014-96-1-1173, and N00014-01-1-0108. Special thanks are extended to R.I. Grove and N.H. Dutrow who modified the wind tunnel and constructed the test section, and to J.A. McConnell, K. Kim, and K.J. Bastyr who helped with the tow tank experiments.

References

Bendat, J.S., Piersol, A.G., 2000. Random Data Analysis and Measurement Procedures, 3rd Edition.. Wiley, New York.

Blackburn, H.M., 1994. Effect of blockage on spanwise correlation in a circular cylinder wake. Experiments in Fluid 1, 134–136.

Corcos, G.M., 1964. The structure of the turbulent pressure field in boundary layer flows. Journal of Fluid Mechanics 18, 353–377.

Gabrielson, T.B., Gardner, D.L., Garrett, S.L., 1995. A simple neutrally buoyant sensor for the direct measurement of particle velocity and intensity in water. Journal of the Acoustical Society of America 97, 2227–2237.

Howe, M.S., Lauchle, G.C., Wang, J., 2001. Aerodynamic lift and drag fluctuations of a sphere. Journal of Fluid Mechanics 436, 41–57.

Kim, H.J., Durbin, P.A., 1988. Observations of the frequencies in a sphere wake and drag increase by acoustic excitation. Physics of Fluids 31, 3260–3265.

Lauchle, G.C., Jones, A.R., 1998. Unsteady lift force on a towed sphere. Journal of Fluids and Structures 12, 949–958.

Maskell, E.C., 1963. A theory of the blockage effects on bluff bodies and stalled wings in a closed wind tunnel. Aeronautical Research Council, R&M No. 3400.

Mceachern, J.F., Lauchle, G.C., 1995. Flow induced noise on a bluff body. Journal of the Acoustical Society of America 97, 947–953.

Wang, J., 1999. Hydrodynamic lift and drag fluctuations of a sphere. Ph.D. Thesis, The Pennsylvania State University, University Park, PA, USA.